

A UNIVERSAL ENTROPY PROFILE FOR THE HOT ATMOSPHERES OF GALAXIES AND CLUSTERS WITHIN R_{2500}

IU. V. BABYK^{1,6,*}, B. R. MCNAMARA^{1,2}, P. E. J. NULSEN^{3,4}, H. R. RUSSELL⁵, A. N. VANTYGHEM¹, M. T. HOGAN^{1,2}, AND F. A. PULIDO¹

¹Department of Physics and Astronomy, University of Waterloo, Waterloo, ON, N2L 3G1, Canada

²Perimeter Institute for Theoretical Physics, Waterloo, ON, N2L 2Y5, Canada

³Harvard-Smithsonian Center for Astrophysics, 60 Garden Street, Cambridge, MA 02138, USA

⁴ICRAR, University of Western Australia, 35 Stirling Hwy, Crawley, WA 6009, Australia

⁵Institute of Astronomy, Madingley Road, Cambridge CB3 0HA, UK

⁶Main Astronomical Observatory of the National Academy of Science of Ukraine, 27 Zabolotnogo Street, Kyiv, 03143, Ukraine

Draft version June 14, 2018

ABSTRACT

We present atmospheric gas entropy profiles for 40 early type galaxies and 110 clusters spanning several decades of halo mass, atmospheric gas mass, radio jet power, and galaxy type. We show that within $\sim 0.1R_{2500}$ the entropy profiles of low-mass systems, including ellipticals, brightest cluster galaxies, and spiral galaxies, scale approximately as $K \propto R^{2/3}$. Beyond $\sim 0.1R_{2500}$ entropy profiles are slightly shallower than the $K \propto R^{1.1}$ profile expected from gravitational collapse alone, indicating that heating by AGN feedback extends well beyond the central galaxy. We show that the $K \propto R^{2/3}$ entropy profile shape indicates that thermally unstable cooling is balanced by heating where the inner cooling and free-fall timescales approach a constant ratio. Hot atmospheres of elliptical galaxies have a higher rate of heating per gas particle compared to central cluster galaxies. This excess heating may explain why some central cluster galaxies are forming stars while most early-type galaxies have experienced no significant star formation for billions of years. We show that the entropy profiles of six lenticular and spiral galaxies follow the $R^{2/3}$ form. The continuity between central galaxies in clusters, giant ellipticals, and spirals suggests perhaps that processes heating the atmospheres of elliptical and brightest cluster galaxies are also active in spiral galaxies.

Subject headings: galaxies: clusters: general galaxies: clusters: intracluster medium

1. INTRODUCTION

Elliptical galaxies, groups, and rich clusters of galaxies are permeated by hot, tenuous atmospheres of plasma that shine in X-rays (Fabian 1994). Hot atmospheres are composed primarily of ionized hydrogen and helium enriched in heavy elements to levels of approximately one third of the Solar value. At their centers, the radiative cooling times fall below $\sim 10^9$ yr, which is much shorter than their ages. Unless heated, hot atmospheres are expected to cool rapidly into cold molecular clouds fueling star formation and powering active nuclei through accretion onto massive nuclear black holes. Maintained in hydrostatic equilibrium with thermal pressure balancing gravity, hot atmospheres capture the energy released by radio jets and the heat and metals ejected by supernova explosions. Hot atmospheres are often contain large scale cavities or bubbles inflated by radio jets launched from massive nuclear black holes (McNamara & Nulsen 2007, 2012; Fabian 2012). The energy released as bubbles rise through the galaxy, heats the hot atmosphere and prevents catastrophic cooling.

The history of cooling and heating by AGN and supernova explosions is encoded in the atmospheric gas entropy (Voit et al. 2002; Voit & Ponman 2003; Voit 2005). Radial entropy profiles are expected to scale as $K \propto r^{1.1}$ where the assembly of hot atmospheres is influenced by gravity alone (Kaiser 1986, 1991; Tozzi & Norman 2001; Voit et al. 2002; Voit & Ponman 2003; Voit et al. 2005; Voit 2005; Reiss & Keshet 2015; Babyk 2016). Departures from this scaling are sensitive to cooling and non-gravitational heating. The radial en-

ropy profile slopes of cluster atmospheres are shallower than $K \propto r^{1.1}$ at $\leq 0.1r_{vir}$ (Ponman et al. 2003; Donahue et al. 2005, 2006; Pratt et al. 2006; Cavagnolo et al. 2009; Walker et al. 2012; Babyk et al. 2014; Panagoulia et al. 2014; Hogan et al. 2017b). The entropy profiles of groups and massive elliptical galaxies also have shallower central slopes (Werner et al. 2012, 2013; Voit et al. 2015), indicating complex thermodynamic histories.

Previous studies revealed a flattening of inner entropy profiles in clusters (Donahue et al. 2005, 2006; Cavagnolo et al. 2009; Voit et al. 2016). By carefully tending to resolution biases, Panagoulia et al. (2014) were the first to show that the broken power law fit where the inner entropy profile follows the form $K \propto r^{0.67}$. Their results were confirmed by Hogan et al. (2017b). In this paper we present atmospheric entropy profiles for 150 systems observed with the *Chandra* X-ray Observatory. Forty are early-type galaxies (elliptical and lenticular galaxies), spiral galaxies, and faint groups. These low-mass systems were combined with 110 central cluster galaxies from Hogan et al. (2017b) and Pulido et al. (2018). We examine the thermodynamic states of hot atmospheres permeating halos with masses between 10^{12} to 10^{15} solar masses and atmospheric gas temperatures spanning 0.4 – 15 keV (Figure 1). The radio jet powers of the systems shown in Figure 1 span $\sim 10^{40}$ – 10^{46} erg s⁻¹. The full X-ray analysis as well as the measurements of thermodynamic properties of low-mass systems, such as temperature, density, cooling time, atmospheric gas mass, and total mass profiles (gas+stars+dark matter) over the radial range ~ 0.1 –50.0 kpc, are presented in Babyk et al. (2018a). We concentrate here on the study of

* babikyura@gmail.com

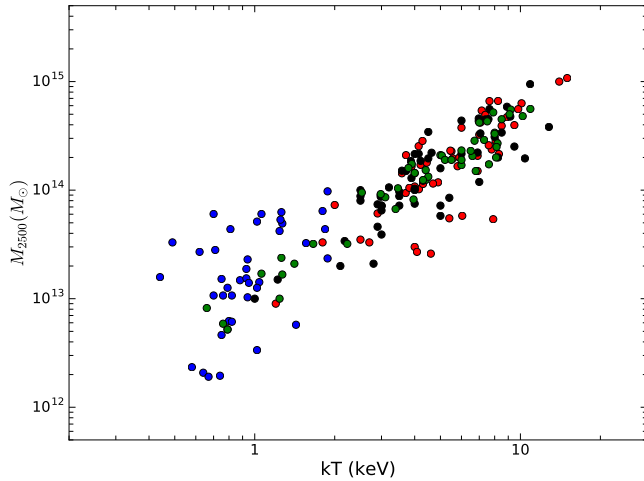


FIG. 1.— The $M_{2500}-T$ relation for the sample of 150 objects spans a wide range of mass and temperature. Data were taken from Hogan et al. (2017b) (red points), Pulido et al. (2018) (black points), Babyk et al. (2018a) (blue points). In addition, we added measurements of Main et al. (2017) (green points) which were obtained for the same objects used in this paper.

entropy profiles obtained in Babyk et al. (2018a).

A Λ CDM cosmology with $\Omega_m = 0.3$, $\Omega_\Lambda = 0.7$, and $H_0 = 70 \text{ km s}^{-1} \text{ Mpc}^{-1}$ is adopted. Errors are quoted at the 1σ confidence level, unless otherwise specified.

2. OBSERVATIONS AND DATA REDUCTION

The sample is drawn from our parent sample (see Babyk et al. 2018b), where 94 early-type galaxies (ETGs) and other low-mass systems observed by the *Chandra* X-ray Observatory were analyzed to investigate X-ray scaling relations. Combining multiple observations where necessary, we selected 40 targets with exposure times exceeding 10 ks and having sufficient counts to build spatially resolved thermodynamic profiles. This selection were performed in Babyk et al. (2018a) where we construct radial profiles of main thermodynamic properties, including temperature, density, cooling time, and mass. Characteristics of the selected targets are presented in Table 1. Complimentary information was obtained from NED², SIMBAD³, and HyperLEDA⁴ databases. Our sample includes 11 brightest cluster galaxies and several spiral galaxies. Angular diameter and luminosity distances were calculated using redshifts or surface brightness fluctuations (Mei et al. 2007), as appropriate.

The *Chandra* X-ray data have been reduced following Hogan et al. (2017b) and Pulido et al. (2018), summarized here. The data were reprocessed and bad pixel files were created using the CIAO V.4.8 software package with the newest version of CALDB V.4.7.1. `chandra_repro` was used to extract the cleaned, level-2 event files. Background flares were removed and a correction was applied for time-dependent gains. Point sources were identified using `wavdetect` and removed. Spectra were then extracted from concentric circular annuli, avoiding bubbles and other asymmetric features, and were deprojected using the DSDEPROJ routine (Sanders & Fabian 2007; Russell et al. 2008).

We use a multi-component spectral model of the form PHABS*(APEC+PO+MEKAL+PO) and XSPEC version 12.9.1

(Arnaud 1996) to fit the deprojected spectra. The spectral model included thermal X-ray emission from the galaxy and its environment (APEC component in our spectral model), unresolved low-mass X-ray binaries (LMXB) (first PO component with slope fixed to 1.6), and other stellar sources (set of MEKAL+PO components with temperature, metallicity, and slope fixed to 0.5 keV, $0.3Z/Z_\odot$, and 1.9, respectively) (see Babyk et al. 2018b,a, for more details). X-ray emission from LMXBs and other stellar sources were modeled as power laws along with the thermal emission from the galaxy. The flux contributed by these sources was usually negligible compared to the thermal emission. However, we study faint systems. Thus, the magnitude and spectral form of the contributions of stellar sources and unresolved low-mass X-ray binaries must be assumed (Boroson et al. 2011; Kim & Fabbiano 2013, 2015). From these fits we derive temperature and electron density profiles which we then use to build entropy profiles.

Clusters with relatively short central cooling times are better fit in the inner regions by two temperature rather than single-temperature thermal models (Panagoulia et al. 2014; Hogan et al. 2017b). Hogan et al. (2017a) and Hogan et al. (2017b) showed that two temperature models are only useful in observations with sufficiently high numbers of photons, and usually when measuring temperatures in projection. We tested the spectra for a second temperature component. Galaxies were refit with a two-temperature model in the form of PHABS*(APEC+APEC+PO+MEKAL+PO). No evidence for a second temperature component was found in any system. As we focus here on deprojected radial profiles of faint systems, we have attempted to fit only single temperature thermal models.

3. MODELLING THE ENTROPY PROFILES

Radial gas entropy profiles were calculated as $K(r) = kT(r)/n_e(r)^{2/3}$, where kT and n_e are the gas temperature and electron density determined by deprojecting a single thermal emission model. The gas entropy profiles for the low-mass systems were compared to those of central cluster galaxies. Entropy profiles of 150 halos are shown in Figure 2. Early-type galaxies/faint groups are shown in blue while clusters are shown in black (Pulido et al. 2018) and red (Hogan et al. 2017b). This figure shows a mean entropy profile over four decades in radius, from the inner 100 parsecs in nearby early-type galaxies to beyond a megaparsec in some galaxy clusters. The right hand panel shows the entropy profile with the radius in units of R_{2500} (within R_{2500} the mean total density is 2500 times the cosmological critical density).

Entropy profiles, in both physical and scaled radial units, extend continuously from galaxy to cluster scales. The low-mass systems and clusters were first modelled separately using a broken power of the form

$$f(x) = \begin{cases} A \cdot (x/x_0)^{\Gamma_1} & \text{if } x \leq x_0 \\ A \cdot (x/x_0)^{\Gamma_2} & \text{if } x > x_0. \end{cases} \quad (1)$$

The entropy profiles in individual galaxies, faint groups, and the centers of clusters are shallower than those at larger radii in clusters. Comparing entropy profiles in physical radii, the normalizations of low-mass systems were found to be 1.5 times larger than cluster normalizations. For the subsequent analysis we have divided the entropies for low-mass systems by 1.5 with respect to cluster profiles when plotted against physical radius, as in Figure 2. This shifts the break radius of the broken power law fitting slightly, but does not affect

² <https://ned.ipac.caltech.edu/>

³ <http://simbad.u-strasbg.fr/>

⁴ Lyon-Meudon Extragalactic Database

TABLE 1
SELECTED LOW-MASS SYSTEMS.

Name	α (J2000) (2)	δ (J2000) (3)	ObsIDs (4)	Exposure ks (5)	Type (6)	BCG (7)	z (8)	D_A Mpc (9)	D_L Mpc (10)	N_H 10^{20} cm^2 (11)	σ_c km/s (12)
IC1262	69.5188	32.0738	6949, 7321, 7322	36.02, 34.98, 35.17	E	✓	0.032649	133.0	141.8	2.47	232±10
IC1459	4.6590	-64.1096	2196	45.14	E3		0.006011	25.503	25.8	1.19	294±6
IC4296	313.5384	27.9729	2021, 3394	19.27, 20.78	E		0.012465	52.358	53.7	4.11	327±5
NGC315	124.5631	-32.4991	4156	39.49	E		0.016485	68.816	71.1	5.87	293±2
NGC499	130.4977	-28.9448	10536	18.33	E		0.014673	61.423	63.2	5.26	253±7
			10865	5.12							
			10866	8.01							
			10867	7.02							
NGC507	130.6430	-29.1326	317	40.30	E	✓	0.016458	68.706	71.0	5.32	292±6
NGC533	140.1457	-59.9683	2880	28.40	E3		0.018509	77.025	79.9	3.12	271±6
NGC708	136.5695	-25.0903	2215, 7921	28.75, 108.63	E	✓	0.016195	67.635	69.8	5.37	222±8
NGC720	173.0194	-70.3572	7372	49.13	E5		0.005821	24.704	25.0	1.55	236±6
			7062	22.12							
			8448	8.06							
			8449	18.91							
NGC741	150.9342	-53.6764	2223	28.14	E0		0.018549	77.186	80.1	4.47	286±9
NGC1316	240.1627	-56.6898	2022	21.21	E		0.005871	24.914	25.2	1.92	224±3
NGC1332	212.1830	-54.3661	2915, 4372	4.10, 16.38	S0		0.005084	21.601	21.8	2.29	313±11
NGC1399	236.7164	-53.6356	9530	56.98	E1	✓	0.004753	20.205	20.4	1.31	334±5
NGC1404	236.9552	-53.5548	16233	91.94	E1		0.006494	27.531	27.9	1.35	228±4
			16231	56.09							
			16232	64.03							
			16234	84.64							
NGC1407	209.6362	-50.3838	14033	50.26	E0		0.005934	25.179	25.5	5.41	265±5
NGC1550	190.9760	-31.8488	5800, 5801	44.55, 44.45	E2	✓	0.012389	52.045	53.3	11.2	300±5
NGC3091	256.7559	27.5029	3215	27.34	E3	✓	0.013222	55.473	56.9	4.75	310±7
NGC3923	287.2759	32.2224	9507	80.90	E4		0.005801	24.620	24.9	6.29	247±6
NGC4073	276.9081	62.3697	3234	25.76	E	✓	0.019584	81.364	84.6	1.90	267±6
NGC4104	204.3284	80.0306	6939	34.86	S0	✓	0.028196	115.60	122.2	1.68	291±6
NGC4125	130.1897	51.3391	2071	52.97	E6		0.004523	19.234	19.4	1.86	238±7
NGC4261	281.8049	67.3726	9569	102.24	E2		0.007378	31.236	31.7	1.56	296±4
NGC4325	279.5840	72.1969	3232	28.30	E4	✓	0.025714	105.80	111.3	2.18	299±78
NGC4374	278.2045	74.4784	5908, 6131	44.04, 35.81	E1		0.003392	16.422	18.1	2.58	275±2
NGC4382	267.7120	79.2372	2016	29.33	S0		0.002432	16.265	17.7	2.51	175±4
NGC4472	286.9222	70.1961	11274	39.67	E2		0.003272	15.621	17.1	1.65	281±3
NGC4552	287.9326	74.9668	13985	49.41	E		0.001134	15.523	16.1	2.56	250±3
			14358	49.41							
			14359	47.11							
NGC4636	297.7485	65.4729	3926, 4415	67.26, 66.17	E0		0.003129	13.335	13.4	1.83	200±3
NGC4649	295.8736	74.3178	8182, 8507	45.87, 15.73	E2		0.003703	15.767	15.9	2.13	329±5
NGC4696	302.4036	21.5580	1560	21.20	E1	✓	0.009867	41.613	42.4	8.07	244±6
NGC4782	304.1379	50.2958	3220	49.33	E0		0.015437	64.545	66.6	3.56	308±11
NGC5044	311.2340	46.0996	17195	77.01	E0	✓	0.00928	39.173	39.9	5.03	226±9
			17196	85.80							
			17653	32.46							
			17654	24.01							
			17666	82.79							
NGC5353	82.6107	71.6336	14903	37.20	S0		0.007755	32.813	33.3	0.98	284±5
NGC5813	359.1820	49.8484	12952	140.00	E1		0.006525	27.662	28.0	4.23	235±3
			12951	71.95							
			12953	31.76							
			13246	45.02							
			13247	34.08							
			13255	43.34							
NGC5846	0.3389	48.9043	7923	85.25	E		0.00491	20.867	21.1	4.24	237±4
NGC6338	85.8062	35.3991	4194	44.52	E5		0.027303	112.10	118.3	2.55	348±40
NGC6482	48.0905	22.9122	3218	10.03	E		0.013129	55.091	56.5	8.04	317±10
NGC6861	350.8772	-32.2109	11752	88.89	SA0		0.009437	39.826	40.6	4.94	407±20
NGC7618	105.5754	-16.9091	16014	121.00	E		0.017309	72.164	74.7	11.9	293±30
UGC408	116.977	-59.40	11389	93.80	SAB		0.014723	61.628	63.5	2.80	198±5

slopes. The normalizations of the entropy profiles with scaled radii were not changed.

Despite the broad range of mass and spatial resolution, Figures 2 and 3 show remarkably uniform profile shapes, although with noticeable variations. The degree to which the variations are due to measurement error, non-uniform exposure level, or real departures from a universal form is unclear. Therefore tests were performed to evaluate the degree to which these systems can be characterized by a single inner power law slope.

3.1. Scatter about the mean entropy profile

We focus on broken power law fits to the entropy profiles of low-mass systems and cool-core clusters. By construction these systems have central cooling times and entropies that fall below 1 Gyr and 30 keV cm², respectively. The entropy profiles are presented in physical units and scaled units as K vs R , K vs R/R_{2500} and K/K_{2500} vs R/R_{2500} . To evaluate the variance, profiles were constructed using three methods.

First, a mean profile was constructed by fitting a broken power law to the entropy values vs. radius for the entire sample. The data along with the best fits in green are shown in Figure 3. We have plotted the inner profile found by Panagoulia et al. (2014) and the outer $K \propto R^{1.1}$ profile for reference. The agreement is good although the outer profile is slightly shallower than $R^{1.1}$.

The broken power-law form was fit to the entropy profiles with both physical and scaled radial units using a simple χ^2 method. Our uncertainties were estimated from the log-likelihood profile following the Wilks theorem. They were computed as the parameter ranges where the log-likelihood does not deviate by more than 1 with respect to its best-fit value. In physical radii the power law slopes were $\Gamma_1 = 0.62 \pm 0.12$ and $\Gamma_2 = 0.95 \pm 0.17$, and the break radius was 14.3 ± 5.2 kpc. For scaled radii the slopes were $\Gamma_1 = 0.69 \pm 0.09$ and $\Gamma_2 = 1.05 \pm 0.14$ and the break radius was $(0.07 \pm 0.02) R/R_{2500}$.

The full results of fitting for unbinned and binned (see below) data, including inner (Γ_1) and outer (Γ_2) slopes, breaks as well as verification test, χ^2 , and probability, p , are given in Table 2. Three different relations, including K vs R , K vs R/R_{2500} , and K/K_{2500} vs R/R_{2500} are presented. K vs R , K vs R/R_{2500} are shown in Figure 3.

Additional power law fits were performed for entropies above and below 50 kpc to compare with Panagoulia et al. (2014). The entropy profiles are characterized by a power law slopes of 1.00 ± 0.16 above 50 kpc and 0.69 ± 0.09 below. These two additional power law models cross at ~ 40 kpc. In Figure 3 (left) we show the entropy profiles predicted from gravitational collapse models, $K(r) \propto r^{1.1}$, as well as those measured below 50 kpc obtained in Panagoulia et al. (2014). Interestingly, Panagoulia et al. (2014) and predicted models cross at ~ 42.5 kpc in agreement with our power law results.

Second, a global mean entropy profile was constructed by averaging the entropy values at each radius, both scaled and physical, for all systems.

The entropy values at each radius were grouped into bins, x_i , and the weighted mean entropy was calculated as $\langle y \rangle = \frac{\sum_i (y_i \times \sigma_i^{-2})}{\sum_i \sigma_i^{-2}}$. The uncertainties of the weighted mean entropy were found as $\sigma_{\langle y \rangle} = \sqrt{\frac{1}{\sum_i \sigma_i^{-2}}}$, where the y_i and σ_i are entropies and their errors, respectively. Assuming that y_i are

normally distributed and independent, the weighted mean is the maximum likelihood estimator. The interval x is 0.03 kpc for physical radius and $0.01R/R_{2500}$ for scaled. The results are presented in Table 2 for three relations and are quoted as ‘‘Binned data’’. The profiles and residuals for three sets of entropies and best-fit modes are shown in Figure 4.

Inspection of Table 2 shows that both approaches give similar results. All slopes agree to within their errors. The mean profile is remarkably tight indicating that the mean slope characterizes the clusters quite well. The second approach (binning) was performed to understand the effects of scatter in the entropy profiles. Both methods agree.

The binned data were fitted for all targets simultaneously and for the low-mass systems and cool-core clusters separately. The central cooling times of non-cool-core objects exceeds ~ 2 Gyr. The corresponding central entropies exceed ~ 50 keV cm². In contrast, the central cooling time and entropy of cool-core clusters lie below 1 Gyr and 30 keV cm², respectively. Non-cool core systems generally do not host central galaxies. Table 2 shows that outer profiles of cool-core and non-cool core clusters are indistinguishable. Both scale roughly as $K \propto R$. The inner profiles of the non-cool core clusters are poorly defined and suffer from low count rates and thus poor statistics. We have therefore not attempted to fit their central regions. Our results for non-cool-core clusters are consistent with previous studies (David et al. 1996; Ponman et al. 1999; David et al. 2001; Ponman et al. 2003; Panagoulia et al. 2014; Hogan et al. 2017b; Pulido et al. 2018).

3.2. Entropy distribution of low-mass systems

Our third approach examines the power-law slopes for each individual low-mass system alone and compares their distribution to the globally-averaged profiles. This analysis is sensitive to understanding fitting biases and real departures from the mean and perhaps their physical cause.

Modeling the entropy profiles individually reveals a relatively broad range of slopes, $\Gamma_1 = 0.2 - 1.2$. Their distribution is presented in bottom plot of Figure 5. The lowest slopes are obtained for NGC499, NGC3923, NGC4125, NGC4382, and UGC408, while the highest are for NGC533, NGC4104, NGC4261, IC4296, and NGC4782. The errors on individual slope measurements shown in Figure 6 are often large compared to the bin size in of the histogram in Figure 5. This indicates that much (but likely not all) of the variance is measurement scatter.

To evaluate this scatter, we combined these systems into five slope bins: <0.3 , $0.3-0.5$, $0.5-0.7$, $0.7-0.9$, and >0.9 , and fit power laws to the means. In the upper panel of Figure 5 we show the results for each separate group. The colors correspond to the individual and binned data as shown. A comparison of the mean profile slopes to the slopes of the individual systems shows that the outlying bins above and below 2/3 are populated primarily by noisy data. For example, the mean slope for the objects falling in the bin 0.1–0.3 includes NGC4125, NGC4325, and UGC408 with power-law slopes 0.20 ± 0.20 , 0.15 ± 0.30 , 0.29 ± 0.43 , respectively. For these the errors on the power law models are large. This is similarly true in the highest bin >0.9 . When averaged, the slope declines to 0.82 ± 0.03 . The upshot is that averaging brings the noisy data closer to the mean value of 2/3. The average slope for these five groups is 0.65 ± 0.06 , consistent with our earlier analysis and consistent with Panagoulia et al. (2014) and Hogan et al. (2017b).

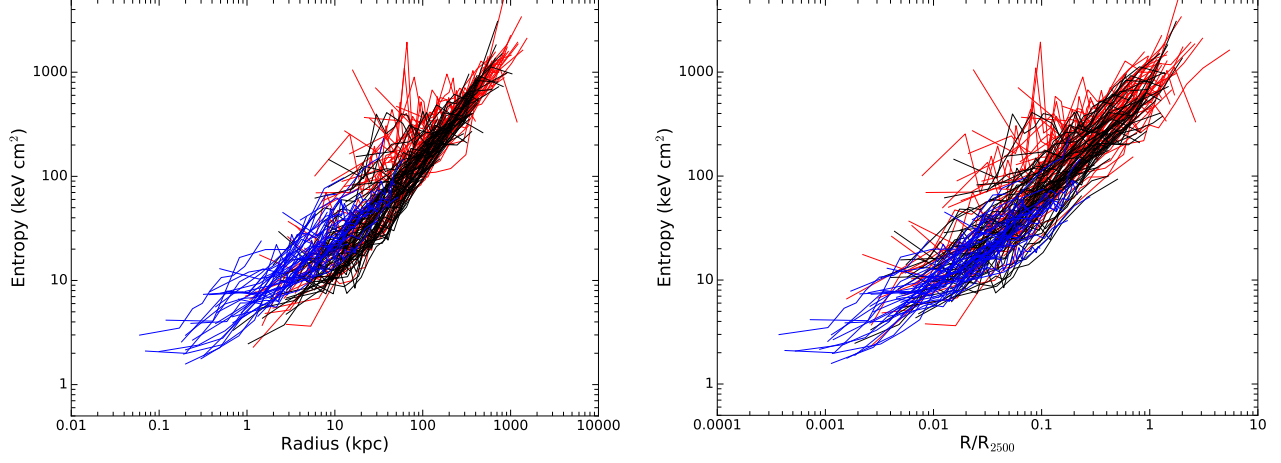


FIG. 2.— Entropy profiles for the sample of clusters, groups and galaxies vs. radius (left) and scaled radius (right). The red profiles are taken from [Hogan et al. \(2017b\)](#), the black profiles are from [Pulido et al. \(2018\)](#), and the blue profiles are from [Babyk et al. \(2018a\)](#). Error bars have been omitted for clarity.

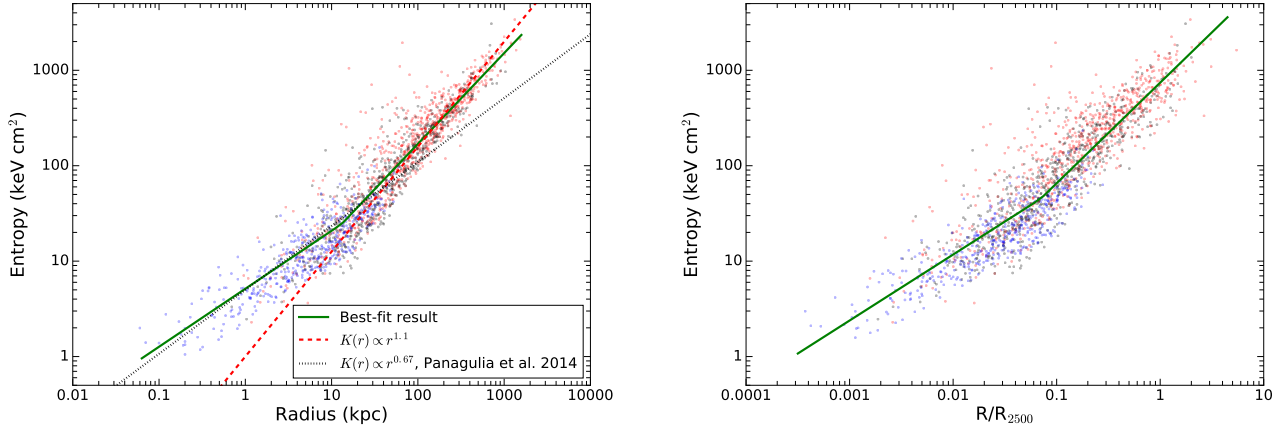


FIG. 3.— The distribution of deprojected radial (left) and radially scaled (right) entropy profiles fitted by the broken power law models discussed in the text. The blue points correspond to the [Babyk et al. \(2018a\)](#) entropy profiles while the red and black points to those entropy profiles derived in [Hogan et al. \(2017b\)](#) and [Pulido et al. \(2018\)](#) respectively. The error bars were deleted for clarity. The red dashed line corresponds to fixed slope $R^{1.1}$ while black dotted line corresponds to a slope of $R^{0.67}$ found by [Panagoulia et al. \(2014\)](#).

TABLE 2

THE BEST-FIT RESULT OF BROKEN POWER LAW FITS (EQ. 1) TO THE ENTROPY PROFILES OBTAINED FOR ENTIRE SAMPLE (ALL) AND FOR LOW-MASS SYSTEMS PLUS COOL-CORE CLUSTERS ONLY (CC+GALAXIES).

Relation	Γ_1	Γ_2	Break kpc	χ^2/dof	p	Data
K vs R	0.62 ± 0.12	0.97 ± 0.17	14.3 ± 5.2	1.5	$\gg 0.0001$	All
K vs R/R_{2500}	0.69 ± 0.09	1.05 ± 0.14	0.07 ± 0.02	1.4	$\gg 0.0001$	All
K/K_{2500} vs R/R_{2500}	0.67 ± 0.09	1.03 ± 0.10	0.07 ± 0.03	1.5	$\gg 0.0001$	All
K vs R	0.65 ± 0.11	1.02 ± 0.11	16.4 ± 5.5	1.3	$\gg 0.0001$	CC+Galaxies
K vs R/R_{2500}	0.64 ± 0.12	0.99 ± 0.15	0.07 ± 0.02	1.3	$\gg 0.0001$	CC+Galaxies
K/K_{2500} vs R/R_{2500}	0.68 ± 0.13	1.02 ± 0.17	0.07 ± 0.02	1.2	$\gg 0.0001$	CC+Galaxies
Binned data						
$K \propto R$	0.68 ± 0.06	0.99 ± 0.11	15.4 ± 3.6	1.1	0.36	All
$K \propto R/R_{2500}$	0.62 ± 0.09	1.05 ± 0.12	0.07 ± 0.02	1.2	0.41	All
$K/K_{2500} \propto R/R_{2500}$	0.71 ± 0.07	1.05 ± 0.09	0.07 ± 0.02	1.2	0.40	All
$K \propto R$	0.65 ± 0.06	1.02 ± 0.10	16.8 ± 3.7	1.2	0.41	CC+Galaxies
$K \propto R/R_{2500}$	0.66 ± 0.08	1.06 ± 0.08	0.07 ± 0.02	1.1	0.32	CC+Galaxies
$K/K_{2500} \propto R/R_{2500}$	0.68 ± 0.09	1.02 ± 0.11	0.07 ± 0.02	1.3	0.45	CC+Galaxies

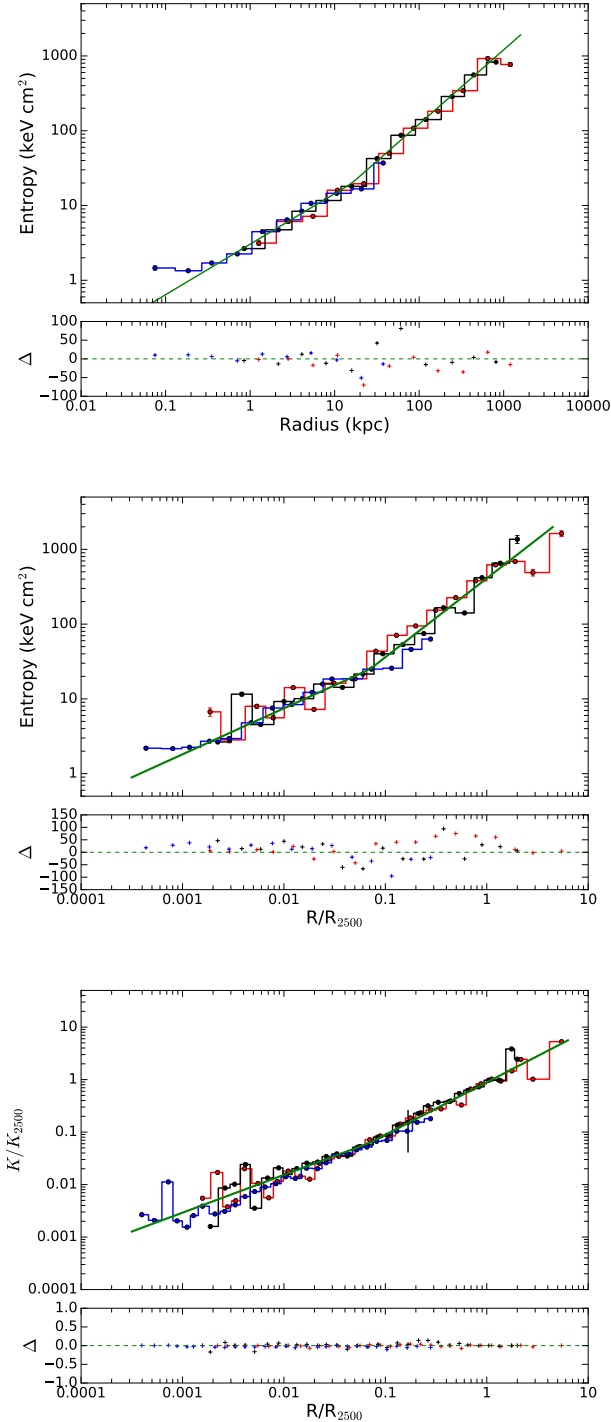


FIG. 4.— The broken power law model fitting, including residuals, of the grouped entropy bins (green lines) for three sets of data. Blue points correspond to low-mass systems while red and black to Hogan et al. (2017b) and Pulido et al. (2018) measurements, respectively.

Despite the very strong evidence for a universal inner profile, a few systems with relatively small errors may depart significantly from the mean. To explore this further we correlated the slopes of individual objects with several physical parameters that may cause the slopes to deviate from the mean.

We explore trends between entropy slope and several physical properties of these systems including central velocity dis-

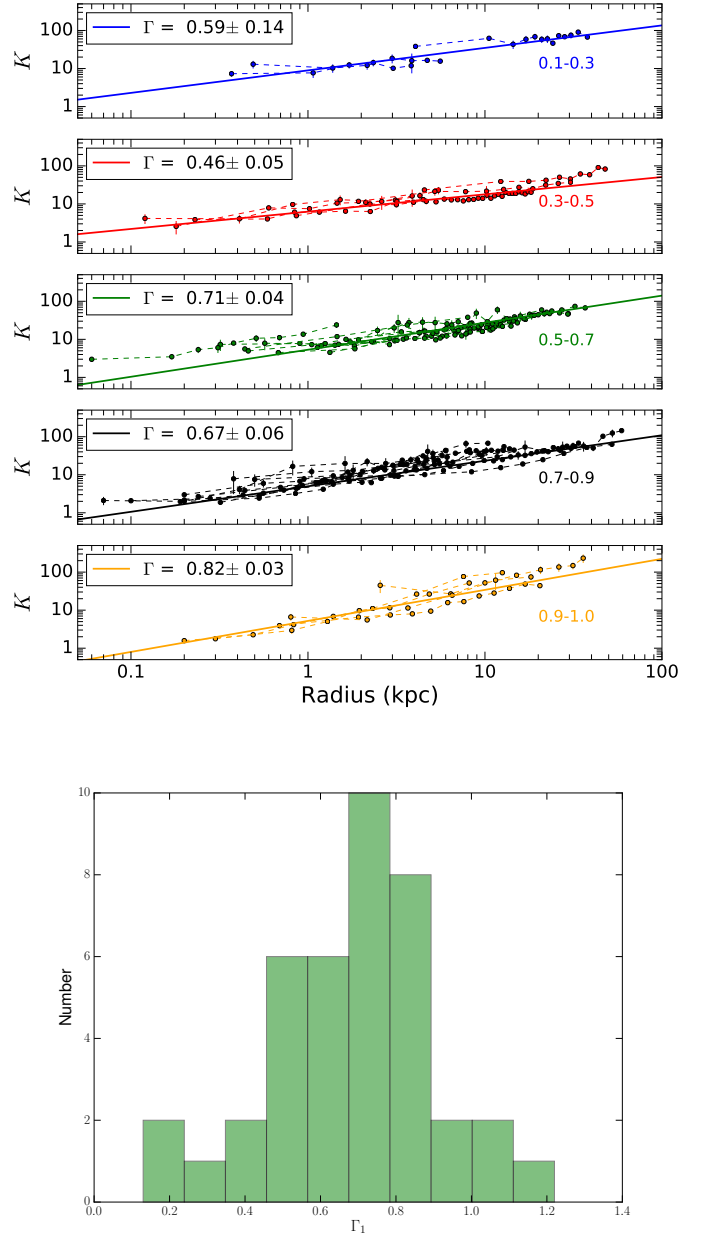


FIG. 5.— (top:) The best-fit results of the simple power law for entire sample of 40 low-mass systems (the entropy is given in $\text{keV} \times \text{cm}^2$; see text for more details). (bottom:) The histogram of best fit slopes for the low-mass sample.

person, optical luminosity, radio flux and luminosity, and AGN cavity power in Figure 6. The velocity dispersions were taken from HyperLEDA while the optical luminosities were taken from Ellis & O’Sullivan (2006); Nagino & Matsushita (2009). Radio fluxes were taken from NED for 1.4 GHz VLA data and converted to radio luminosity using $L = S \times 4\pi \times D_L^2 \times \nu$. Here S is the radio flux, D_L is the luminosity distance, and ν is the frequency. The radio luminosities were converted to mechanical feedback cavity power using the Cavagnolo et al. (2010) scaling relation.

Figure 6 shows the trends. No clear correlation emerges between entropy profile slope and radio luminosity, mechanical power, stellar velocity dispersion, or galaxy luminosity. For reference the mean slope and its 1σ and 2σ confidence in-

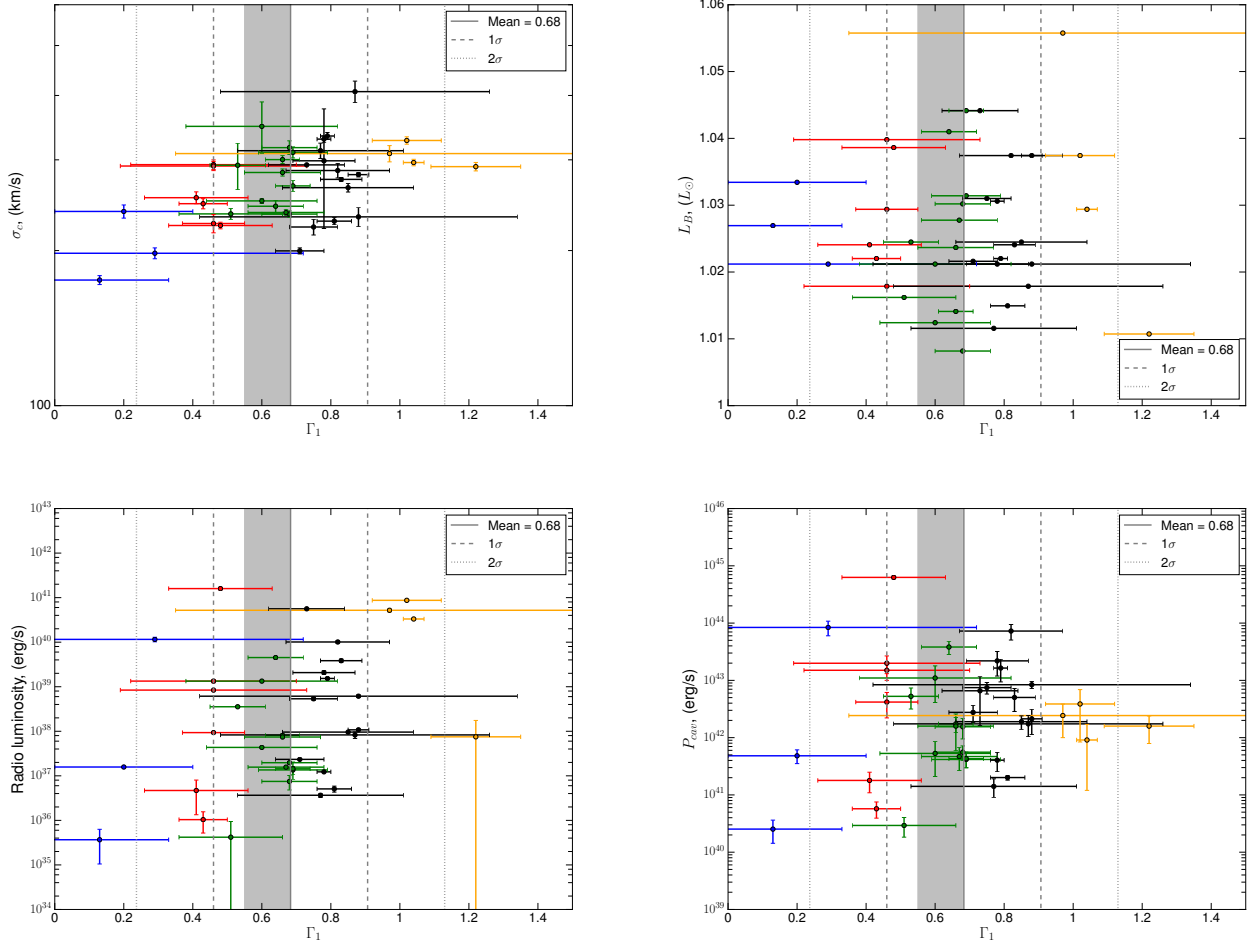


FIG. 6.— The correlations of individual best-fit slopes with central velocity dispersion, optical and radio luminosities as well as cavity power for low-mass systems. The shaded areas correspond to the best-fit result with 1σ uncertainty for all 40 systems, while vertical solid lines with dashed and dotted lines correspond the mean and its 1 and 2 σ confidence levels, respectively. The colors of points are the same as given on previous plot.

tervals are shown. The best-fit power law slope 0.62 ± 0.09 obtained for all low-mass systems, with 1σ uncertainty are indicated by the shaded areas in Figure 6.

The ranges of velocity dispersion and optical luminosity are limited and thus have little leverage. However the range of radio luminosity spans ~ 6 orders of magnitude. This is noteworthy because AGN outbursts can have a dramatic effect on hot atmospheres as they deposit enormous amounts of energy. Yet even the largest outburst have little impact on the central gas density profiles (Hogan et al. 2017b; McNamara et al. 2016). This is also true for entropy. Central entropy profile slopes remain close to $R^{2/3}$ regardless of AGN power. This is inconsistent with many feedback models (cf., Hogan et al. (2017b); Pulido et al. (2018)).

3.3. Entropy profiles for S0 and S galaxies

The six lenticular and spiral galaxies in our sample have prominent dust disks. X-ray and optical images of two of the most prominent lenticular and spiral galaxies are shown in Figure 7.

Despite being spiral galaxies, they are bright X-ray sources that permit their entropy profiles to be measured. Their entropy profiles shown in Figure 8 have similar slopes ($\Gamma = 0.74 \pm 0.06$) to the elliptical and brightest cluster galaxies ($\Gamma = 0.62 \pm 0.09$). This is significant as it links the thermody-

namic properties of their atmospheres across galaxy morphology and halo mass. It indicates that the underlying physics that imprints the entropy distributions in elliptical and spiral galaxies is similar.

4. DISCUSSION

Consistent with many previous studies, we have shown that the entropy profiles of galaxies and clusters can be described by a broken power law. The inner profiles for central galaxies of all types, including spirals, is characterized by $K \propto R^{2/3}$, with only small variations. At large radii, between $\sim 0.1 - 1R_{2500}$, $K \propto R$. The gas entropy in the outer parts of cluster atmospheres imprinted primarily by gravitational collapse is expected to follow $K \propto R^{1.1}$ (Voit et al. 2002; Voit & Ponman 2003; Voit 2005; Cavagnolo et al. 2008). Our outer profiles are slightly shallower.

The $K \propto R^{2/3}$ inner slope reflects higher gas entropy than expected from an inward extrapolation of the $K \propto R^{1.1}$ profile. Higher central gas entropy indicates additional heating of the atmosphere in the vicinity of the central galaxy. Recent studies have shown that when resolution effects are properly accounted for, the inner entropy profile in clusters can be described as $K \propto R^{2/3}$ (Panagoulia et al. 2014; Hogan et al. 2017b). The $R^{2/3}$ form is significant as we shall see below.

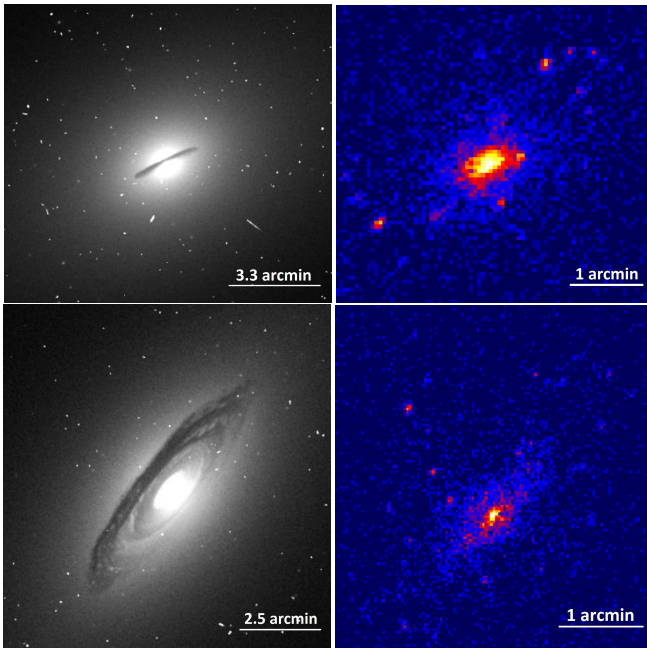


FIG. 7.— 5439.0 Å Hubble Space Telescope (left) and 0.5–7.0 keV *Chandra* (right) images of the S0 (NGC1332) and SA0 (NGC6861) galaxies.

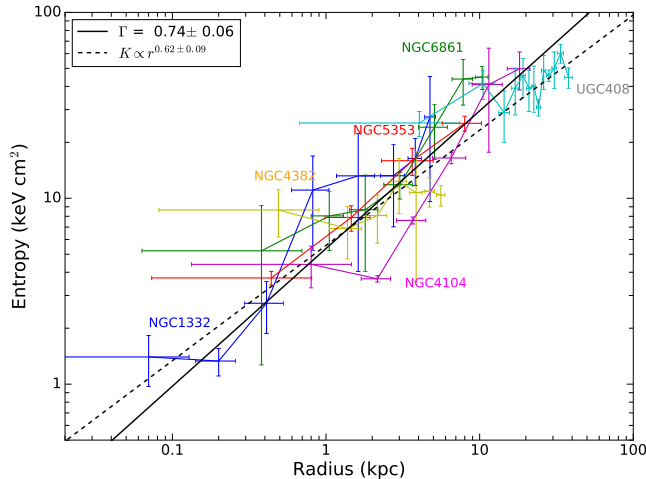


FIG. 8.— Deprojected entropy profiles with the best-fit slope (solid line) for the lenticular and spiral galaxies. The best-fit slope for the entire sample (dashed line) is shown for comparison. The S0 and S galaxies follow the same slope as the ellipticals.

How does this broken power-law form arise? When hot atmospheres are heated by radio jets launched by central black holes or by supernova explosions, they do not necessarily respond with a large temperature rise. Instead, heating raise the entropy of the gas, causing it to expand and lift outward. Since gravity is weaker at larger radii, the weight of the gas is reduced causing the pressure to decrease. As a result, most of the heat energy is converted into gravitational potential energy, rather than thermal energy. Conversely, as the atmosphere cools and its entropy decreases, the gas contracts and moves inward, again with little change in the gas temperature. Under the right conditions, some thermally unstable gas can cool faster than the rest, condensing into molecular clouds that form stars and feed the nuclear black hole. The entropy parameter encodes information about the heating and cooling

history of hot atmospheres.

The break to a shallower inner slope seen in Figure 3 may mark the boundary, within which the atmosphere is strongly heated by the radio jets. Remarkably, early-type galaxies including spirals and central galaxies of massive clusters follow the same $R^{2/3}$ form. This indicates that the $R^{2/3}$ form is linked to the central galaxy.

Assuming the central galaxy is an isothermal sphere, i.e., $M = 2\sigma^2 R/G$, the free-fall time is $t_{\text{ff}} = R/\sigma$. Cooling time scales as $t_c \propto K^{3/2}/(\Lambda\sqrt{kT})$ so, for $K \sim R^{2/3}$, the ratio of cooling time to free-fall time scales as $t_c/t_{\text{ff}} \propto \sigma/(\Lambda\sqrt{kT})$. Here, σ is the stellar velocity dispersion, R is the radius, G is the gravitational constant, and Λ is the cooling function (Hogan et al. 2017b). This expression has no radial dependence, which is noteworthy. It implies that t_c/t_{ff} becomes constant where gas becomes thermally unstable.

The ratio t_c/t_{ff} is understood to be related to the condition leading to thermally unstable atmospheric cooling. The cooling time is defined as the time it takes for atmospheric gas to radiate away its thermal energy. It is expressed here by

$$t_c = \frac{3p}{2n_e n_H \Lambda(Z, T)} \approx \frac{3pV}{2L_X}, \quad (2)$$

where $p = 2n_e k_B T$ is the gas pressure, $\Lambda(Z, T)$ is the cooling function, depends on metallicity and temperature, and L_X is the X-ray luminosity. The free-fall time was given by

$$t_{\text{ff}}(r) \simeq \sqrt{2r/g}, \quad (3)$$

where $g = (GM)/r^2$ is the local gravitational acceleration and the total mass, M , was taken from our mass profiles (Babyk et al. 2018a).

Hot atmospheres are expected to become thermally unstable to linear density perturbations when the ratio of t_c/t_{ff} falls below unity (Nulsen 1986; Pizzolato & Soker 2005; McCourt et al. 2012). This criterion is never achieved in static hot atmospheres. Nevertheless, molecular gas and star formation are observed in central cluster galaxies indicating that thermally unstable cooling is occurring. Recent studies have suggested that this instability criterion may rise well above unity, so that thermally unstable cooling can ensue from linear perturbations when t_c/t_{ff} falls below 10 (Sharma et al. 2012; McCourt et al. 2012; Gaspari & Churazov 2013; Li et al. 2015; Voit & Donahue 2015). McCourt et al. (2012) argued that this condition was met in systems whose central galaxies contained significant levels of cold gas.

However, more recent analyses of cluster central galaxies paying close attention to mass profile measurements and resolution effects have revealed no evidence that t_c/t_{ff} falls significantly below 10 in any system, including those that are thermally unstable (McNamara et al. 2016; Hogan et al. 2017b; Pulido et al. 2018). Instead, these studies found that t_c/t_{ff} lies between about 10 and 30 in systems with star formation and molecular clouds. In addition, lower values of t_c/t_{ff} do not correlate with higher star formation rates or molecular gas masses. Consistent with Voit et al. (2015), they found a floor at $t_c/t_{\text{ff}} \sim 10$ rather than a threshold. While this floor may well be physically significant, the range of t_c/t_{ff} values can be explained as an observational selection effect (Hogan et al. 2017a). Furthermore, newer simulations have shown that the physical bases for the t_c/t_{ff} criterion is invalid, and that thermally unstable cooling may occur over a much larger parameter space (Choudhury & Sharma 2016). While it is clear that

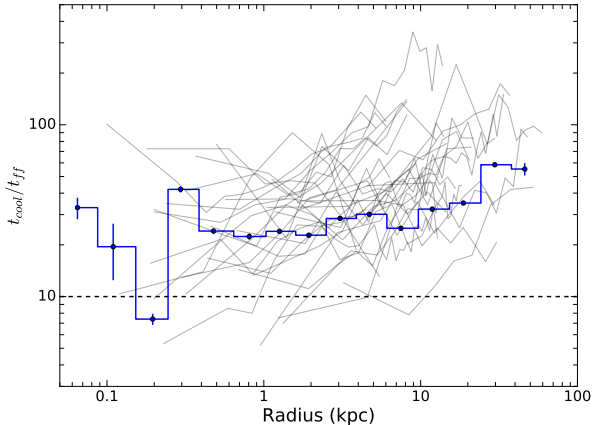


FIG. 9.— Deprojected t_c/t_{ff} profiles (gray shaded lines) for entire sample of low-mass systems along with the average t_c/t_{ff} profile (blue line). The error bars of t_c/t_{ff} profiles have been omitted for clarity.

the cooling time of the hot atmosphere is correlated with the presence or absence of thermally unstable cooling, the ratio t_c/t_{ff} in clusters does not. Here we perform a similar analysis on the atmospheres of giant elliptical galaxies.

The ratio t_c/t_{ff} for objects in our sample is shown in Figure 9. The t_c/t_{ff} profiles were binned in the same way as the entropy profiles, and an average profile was computed. We see that average profile is constant over all radii, with the exception of few outliers seen in the first couple bins. This is likely resolution effect. Nevertheless, the minimum t_c/t_{ff} , including the average profile, never falls significantly below 10 in the targets, but instead lies between 10 and nearly 100. The average profile lies close to 30, which is in agreement with t_c/t_{ff} profiles obtained for galaxy clusters (Hogan et al. 2017b; Pulido et al. 2018). Analyses that properly account for the gravity of the central galaxy and for resolution biases, including the data analyzed in Werner et al. (2012); Voit et al. (2015); Hogan et al. (2017b); Pulido et al. (2018), have found that t_c/t_{ff} always exceeds 10. This is true in atmospheres that are demonstrably cooling into molecular clouds. Therefore, $t_c/t_{\text{ff}} \lesssim 10$ is not a threshold for thermal instability (Hogan et al. 2017b; Pulido et al. 2018; Babyk et al. 2018a). It instead indicates the degree to which the bulk of the atmosphere is thermodynamically stable.

The closer this ratio is to unity, the more susceptible the atmosphere becomes to thermally unstable perturbations. For example, perturbations introduced as gas is lifted by radio bubbles are linked to thermally unstable cooling (Pizzolato & Soker 2005; McCourt et al. 2011; McNamara et al. 2016). Atmospheric gas lifted outward by a galaxy collision or turbulence may also trigger thermally unstable cooling. For the inner region where the entropy varies as $R^{2/3}$, t_c/t_{ff} is approximately constant. This is the region most susceptible to perturbations that promote thermally unstable cooling.

The entropy slope within $\sim 0.1R_{2500}$ indicates that the cooling time of the atmosphere, which rises with radius, is in close balance with the heating timescale, i.e., $t_c \sim t_H$. As thermally unstable gas cools and leaves the hot atmosphere, the mean entropy of the remaining hot gas rises. The cooling gas then fuels the active nucleus which raises the entropy leading to the inner floor in t_c/t_{ff} . At larger radii where the entropy reaches $K \sim R^{1.1}$, the cooling time exceeds 10^9 yr. The slightly shall-

lower slope we find indicates that heating by AGN may be important at altitudes approaching R_{2500} .

The break radius of $0.1R_{2500}$ corresponds to linear scales of 20–40 kpc in central cluster galaxies, which is indeed the region where thermally unstable cooling leads to nebular line emission (McDonald 2011), molecular gas (Edge et al. 2002), and star formation proceeding at tens of solar masses per year (O’Dea et al. 2008). However, this radius is smaller, ~ 15 kpc, in early-type galaxies. Unlike central cluster galaxies, early-type galaxies contain much lower levels of molecular gas. They rarely form stars at significant rates (Werner et al. 2014) despite having similar entropy profiles.

4.1. Why are Elliptical Galaxies Dormant?

Why most early-type galaxies lie dormant, despite short central cooling times, while some central cluster galaxies are burgeoning is puzzling. The reasons are twofold. First, the hot atmospheres of early-type galaxies/groups contain less mass than those in clusters. Therefore, their fuel reservoirs are smaller. Second, the active nuclei in lower mass, early-type galaxies supply more energy per gas particle than the active nuclei of central cluster galaxies. Central cluster galaxies with cooling atmospheres have typical jet powers and gas masses within $0.1R_{2500}$ of $P_{\text{jet}} \approx 10^{43}$ erg/s and $M_g \approx 10^{12} M_\odot$, respectively. The energy absorbed per gas particle, $\epsilon = \eta E_{\text{tot}} \mu m_p / M_g$ (Ma et al. 2011), is then ~ 0.1 keV/particle. Here $\mu = 0.63$ is the mean molecular weight of the gas. $\eta \simeq 0.1$ is an efficiency factor that accounts for the fraction of the jet’s enthalpy that heats the atmosphere and the fraction of the bubble enthalpy deposited in the inner region (Weinberger et al. 2017). In many systems, this level of heating cannot quite keep up with the rate of cooling, leading to significant star formation.

On the other hand, for early-type galaxies/groups with average jet powers of $P_{\text{jet}} \approx 10^{41-42}$ erg/s, and atmospheric gas masses, $M_g \approx 10^9 M_\odot$ within $0.1R_{2500}$, we find an average heating level of $\sim 1-10$ keV/particle. We have further assumed all systems have been active at the same level for 10 Gyr, and we have ignored radiative cooling.

While crude, these calculations indicate that the level of heating per gas particle by active nuclei in early-type galaxies generally exceeds that in groups and clusters. Apparently active nuclei in early-type galaxies are better able to prevent significant levels of star formation while allowing enough cooling near the nucleus to maintain the energetic feedback loop.

The similarity in entropy profile shape across such an enormous range of jet power, halo mass, and atmospheric gas mass is significant. It indicates that the AGN feedback mechanism is extraordinarily responsive and gentle. At the same time, the atmosphere is able to maintain a rough balance between heating and cooling throughout the entire $K \propto R^{2/3}$ cooling region. This represents a deep challenge to hydrodynamic simulations, which generally show dramatic time variations in the temperature, density, and entropy profiles in response to radio jet interactions (Gaspari et al. 2012; Sijacki et al. 2011). The active nucleus must respond promptly to heating and cooling over the entire $0.1R_{2500}$ region without inducing large entropy excursions in response to the jet (Gaspari et al. 2012; Sijacki et al. 2011; Weinberger et al. 2017). This is a general result that extends throughout the elliptical galaxy mass range including spiral galaxies.

5. SUMMARY

We have presented new entropy profiles of 40 elliptical galaxies, spiral galaxies, and faint groups of galaxies, and we

compared them to 110 entropy profiles of cool-core and non-cool-core galaxy clusters observed by *Chandra* X-ray Observatory. The entropy profiles cover a wide range of temperature, total mass, gas mass, radio, and central galaxy optical luminosity, and jet power. Our results are summarized as follows:

- The entropy profiles within $\sim 0.1R_{2500}$ of elliptical, lenticular, early spiral, and brightest cluster galaxies, follow approximately as $K \propto R^{2/3}$.
- Beyond $0.1R_{2500}$ entropy profiles are slightly shallower than $K \propto R^{1.1}$, indicating that heating, likely by AGN feedback, extends well beyond the central galaxy.
- This sample includes 22 non-cool core clusters. Four are centered on a bright galaxy; 18 are not. The central entropy values of non-cool core clusters with and without BCGs lie above $\sim 50 \text{ keV cm}^2$. Their entropy profiles, though not well defined due to poor photon statistics, are shallower than the $R^{2/3}$ form seen in cool-core clusters that contain central galaxies. The outer entropy profiles of non-cool core clusters follow the $R^{1.1}$ profile beyond $\sim 0.1R_{2500}$, similarly to cool core clusters. It is not clear how the $R^{2/3}$ form arises. Does it depend on the central galaxy alone or the existence of a central galaxy residing in a cooling atmosphere stabilized by feedback? The data thus far suggest the latter. Additional study is needed to clarify the issue.

- The $K \propto R^{2/3}$ entropy profile shape is intimately related to the central galaxy itself and is consistent with thermally unstable cooling balanced by heating where the inner cooling and free-fall timescales approach a constant ratio.
- Hot atmospheres of early-type galaxies are heated at a higher rate per gas particle than central cluster galaxies. The extra heating may explain at least in part why early-type galaxies are largely dormant.

BRM acknowledges funding from the Natural Science and Engineering Research Council of Canada and from the Canadian Space Agency. Support for this work was provided in part by the National Aeronautics and Space Administration through Chandra Award Number G07-18104X (Cen A) issued by the Chandra X-ray Observatory Center, which is operated by the Smithsonian Astrophysical Observatory for and on behalf of the National Aeronautics Space Administration under contract NAS8-03060. The scientific results reported in this article are based on observations made by the Chandra X-ray Observatory and has made use of software provided by the Chandra X-ray Center (CXC) in the application packages CIAO, ChIPS, and Sherpa. This research has also made use of the NASA/IPAC Extragalactic Database (NED).

REFERENCES

- Arnaud, K. A. 1996, in *Astronomical Society of the Pacific Conference Series*, Vol. 101, *Astronomical Data Analysis Software and Systems V*, ed. G. H. Jacoby & J. Barnes, 17
- Babyk, I. 2016, *Astronomy Reports*, 60, 542
- Babyk, I., McNamara, B., Hogan, M., et al. 2018a, in prep.
- Babyk, I. V., McNamara, B. R., Nulsen, P. E. J., et al. 2018b, *ApJ*, 857, 32
- Babyk, Y. V., Del Popolo, A., & Vavilova, I. B. 2014, *Astronomy Reports*, 58, 587
- Borson, B., Kim, D.-W., & Fabbiano, G. 2011, *ApJ*, 729, 12
- Cavagnolo, K. W., Donahue, M., Voit, G. M., & Sun, M. 2008, *ApJ*, 683, L107
- . 2009, *ApJS*, 182, 12
- Cavagnolo, K. W., McNamara, B. R., Nulsen, P. E. J., et al. 2010, *ApJ*, 720, 1066
- Choudhury, P. P., & Sharma, P. 2016, *MNRAS*, 457, 2554
- David, L. P., Jones, C., & Forman, W. 1996, *ApJ*, 473, 692
- David, L. P., Nulsen, P. E. J., McNamara, B. R., et al. 2001, *ApJ*, 557, 546
- Donahue, M., Horner, D. J., Cavagnolo, K. W., & Voit, G. M. 2006, *ApJ*, 643, 730
- Donahue, M., Voit, G. M., O’Dea, C. P., Baum, S. A., & Sparks, W. B. 2005, *ApJ*, 630, L13
- Edge, A. C., Wilman, R. J., Johnstone, R. M., et al. 2002, *MNRAS*, 337, 49
- Ellis, S. C., & O’Sullivan, E. 2006, *MNRAS*, 367, 627
- Fabian, A. C. 1994, *ARA&A*, 32, 277
- . 2012, *ARA&A*, 50, 455
- Gaspari, M., Brighenti, F., & Temi, P. 2012, *MNRAS*, 424, 190
- Gaspari, M., & Churazov, E. 2013, *A&A*, 559, A78
- Hogan, M. T., McNamara, B. R., Pulido, F., et al. 2017a, *ApJ*, 837, 51
- Hogan, M. T., McNamara, B. R., Pulido, F. A., et al. 2017b, *ApJ*, 851, 66
- Kaiser, N. 1986, *MNRAS*, 222, 323
- . 1991, *ApJ*, 383, 104
- Kim, D.-W., & Fabbiano, G. 2013, *ApJ*, 776, 116
- . 2015, *ApJ*, 812, 127
- Li, Y., Bryan, G. L., Ruszkowski, M., et al. 2015, *ApJ*, 811, 73
- Ma, C.-J., McNamara, B. R., Nulsen, P. E. J., Schaffer, R., & Vikhlinin, A. 2011, *ApJ*, 740, 51
- Main, R. A., McNamara, B. R., Nulsen, P. E. J., Russell, H. R., & Vantghem, A. N. 2017, *MNRAS*, 464, 4360
- McCourt, M., Parrish, I. J., Sharma, P., & Quataert, E. 2011, *MNRAS*, 413, 1295
- McCourt, M., Sharma, P., Quataert, E., & Parrish, I. J. 2012, *MNRAS*, 419, 3319
- McDonald, M. 2011, *ApJ*, 742, L35
- McNamara, B. R., & Nulsen, P. E. J. 2007, *ARA&A*, 45, 117
- . 2012, *New Journal of Physics*, 14, 055023
- McNamara, B. R., Russell, H. R., Nulsen, P. E. J., et al. 2016, *ApJ*, 830, 79
- Mei, S., Blakeslee, J. P., Côté, P., et al. 2007, *ApJ*, 655, 144
- Nagino, R., & Matsushita, K. 2009, *A&A*, 501, 157
- Nulsen, P. E. J. 1986, *MNRAS*, 221, 377
- O’Dea, C. P., Baum, S. A., Privon, G., et al. 2008, *ApJ*, 681, 1035
- Panagoulia, E. K., Fabian, A. C., & Sanders, J. S. 2014, *MNRAS*, 438, 2341
- Pizzolato, F., & Soker, N. 2005, *ApJ*, 632, 821
- Ponman, T. J., Cannon, D. B., & Navarro, J. F. 1999, *Nature*, 397, 135
- Ponman, T. J., Sanderson, A. J. R., & Finoguenov, A. 2003, *MNRAS*, 343, 331
- Pratt, G. W., Arnaud, M., & Pointecouteau, E. 2006, *A&A*, 446, 429
- Pulido, F. A., McNamara, B. R., Edge, A. C., et al. 2018, *ApJ*, 853, 177
- Reiss, I., & Keshet, U. 2015, *ApJ*, 810, 129
- Russell, H. R., Sanders, J. S., & Fabian, A. C. 2008, *MNRAS*, 390, 1207
- Sanders, J. S., & Fabian, A. C. 2007, *MNRAS*, 381, 1381
- Sharma, P., McCourt, M., Quataert, E., & Parrish, I. J. 2012, *MNRAS*, 420, 3174
- Sijacki, D., Springel, V., & Haehnelt, M. G. 2011, *MNRAS*, 414, 3656
- Tozzi, P., & Norman, C. 2001, *ApJ*, 546, 63
- Voit, G. M. 2005, *Reviews of Modern Physics*, 77, 207
- Voit, G. M., Bryan, G. L., Balogh, M. L., & Bower, R. G. 2002, *ApJ*, 576, 601
- Voit, G. M., & Donahue, M. 2015, *ApJ*, 799, L1
- Voit, G. M., Donahue, M., O’Shea, B. W., et al. 2015, *ApJ*, 803, L21
- Voit, G. M., Kay, S. T., & Bryan, G. L. 2005, *MNRAS*, 364, 909
- Voit, G. M., Meece, G., Li, Y., et al. 2016, *ArXiv e-prints*, arXiv:1607.02212
- Voit, G. M., & Ponman, T. J. 2003, *ApJ*, 594, L75
- Walker, S. A., Fabian, A. C., Sanders, J. S., & George, M. R. 2012, *MNRAS*, 427, L45
- Weinberger, R., Ehlert, K., Pfrommer, C., Pakmor, R., & Springel, V. 2017, *MNRAS*, 470, 4530
- Werner, N., Allen, S. W., & Simionescu, A. 2012, *MNRAS*, 425, 2731

Werner, N., Urban, O., Simionescu, A., & Allen, S. W. 2013, *Nature*, 502, 656

Werner, N., Oonk, J. B. R., Sun, M., et al. 2014, *MNRAS*, 439, 2291